Supporting Info

Single-Step Nanoporation of Water-Immersed Polystyrene Film by Gaseous Nanobubbles

Hana Tarábková and Pavel Janda*

J.Heyrovský Institute of Physical Chemistry, Czech Academy of Sciences, v.v.i.

Dolejškova 3, Prague, CZ 182 23, Czech Republic

1. Nanobubble imaging and identification

Surface gaseous nanobubbles form more or less dense assemblies on water-immersed surfaces (Figure S1). Their identification and distinguishing from solid nano-objects can be provided by in-situ AFM imaging in a phase shift or deflection mode. We have utilized cantilever deflection mapping technique (for details see our former paper[1]), which identifies nanobubbles (NB) as elastic objects, characteristic by attractive capillary (bridging) forces between the AFM tip and nanobubble interface[2-5]. These forces cause lowering cantilever deflection, down to even negative values (downward bending) compared to positive deflection on solid objects. Figures S1A,C show in-situ AFM (tapping) height image of surface gaseous nanobubble assembly, while

Figures S1B,D show the same assembly in deflection mode, where lowered/negative cantilever deflection signal clearly distinguishes surface from surrounding solid surface.

A   B

C   D
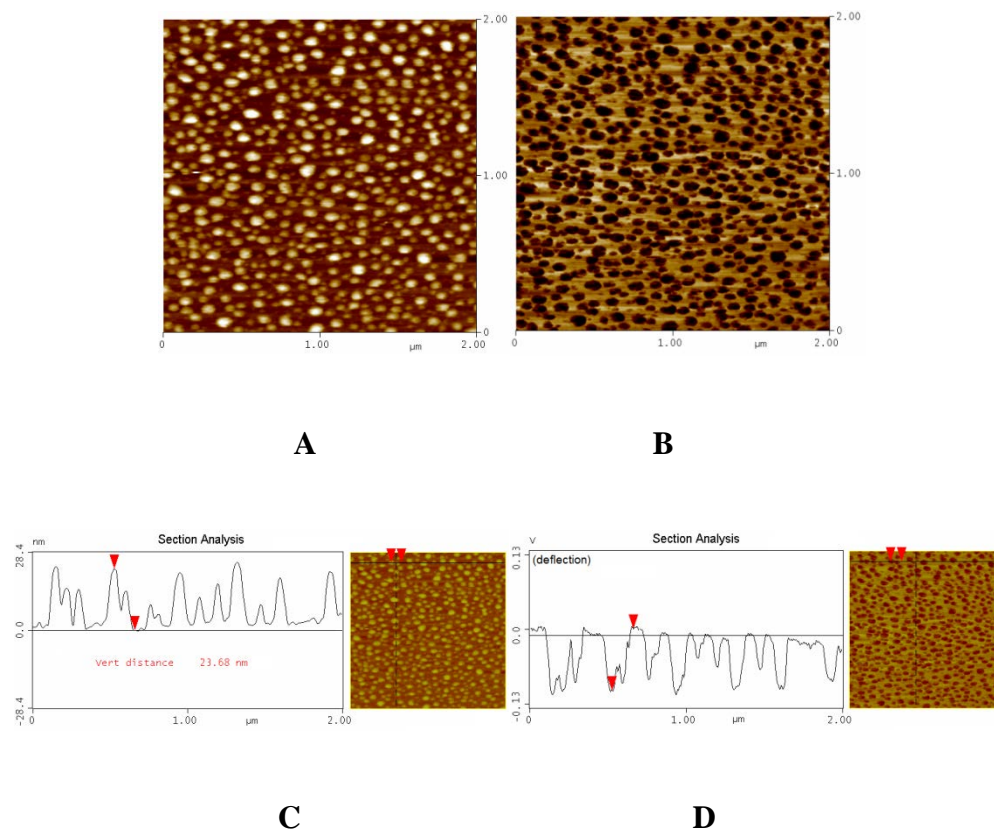
Figure S1. In situ tapping AFM image, height (A) and deflection (B) of surface nanobubbles in deionized water. While topography (height) image does not distinguish nanobubbles from solid objects, cantilever deflection mapping clearly identifies nanobubbles as elastic objects on which the deflection drops due to attractive bridging forces causing negative cantilever bending. Corresponding identical profile (line) analyses of height (C) and cantilever deflection signal in volts (D). For technical details, see ref[6].

Typical surface nanobubble dimensional distributions are shown in Figure S2.

A   **B**
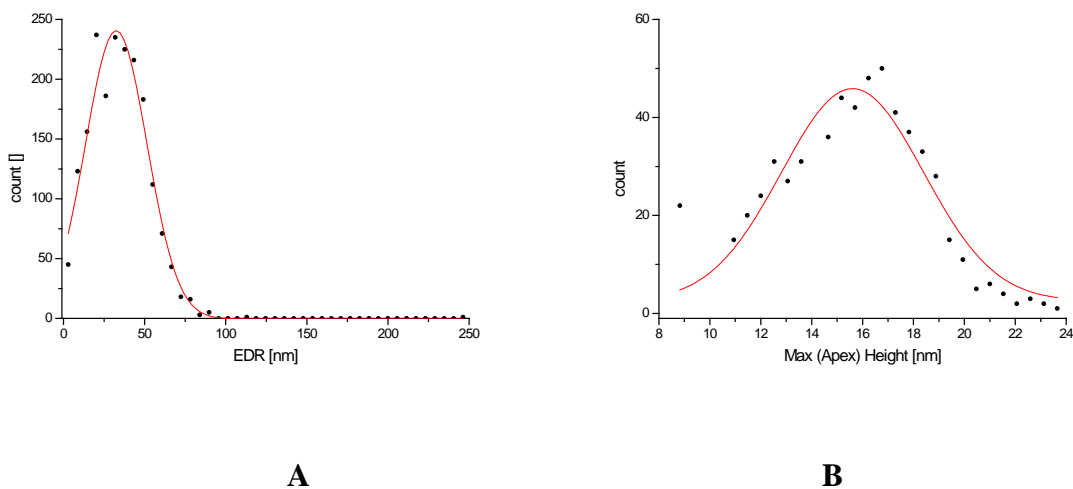
Figure S2: Typical dimensional distributions of surface gaseous nanobubbles: Nanobubble Radius (expressed as Equivalent Disk Radius, EDR) distribution plot (A) and Maximum (Apex) Height distribution plot (B). Black dots represent experimental data, red curves - best fits (Gauss). All dimensions are acquired from in situ AFM (tapping, height) images. AFM image data were processed by the SPM Data Visualization and Analysis Tool Gwyddion v. 2.43.

The surface nanobubble assembly by no means represents rigid, stationary system and AFM, by its nature, is relatively slow and intrusive imaging technique, where the tip interacts with surface nanobubble affecting its nanomorphology during scanning[7]. It has been proven that decreased tapping setpoint (increased scan load) by about 30% causes NB coalescence, resulting in significantly decreased (by more than 80%) number of NBs, increased NB lateral size and hence increased NB-covered surface area[8].

The modulated AFM tip−nanobubble interaction causes, especially in tapping mode, repetitive expansion, compression (height lowering) and lateral displacement[7], which also renders the nanobubble coalescence[9,10] and tip-induced ripening, particularly in dense nanobubble assemblies shown in Figure S1.

2. The stability of nanobubble imprints in polystyrene film

The nanobubble-assisted nanostructuring of polystyrene film is performed during its water-immersion in a process triggered by a mild (-10 kPa) short (5 sec) pressure drop. Once nanostructures are formed on polystyrene surface, they are stable after emersion from water, withstand 24 hours drying at room temperature in ambient atmosphere (air) and even 2-hour drying in vacuum (50 Pa/25°C) without any change in nanomorphology, as illustrated in Figure S3.

These results further confirm presented model of nanoprotrusions as solid (polystyrene-filled, not hollow) convex nanostructures created by squeezing and pushing polystyrene within pinned nanobubble circular contact line once tension stress developed by expanding nanobubble exceeds the polystyrene elasticity threshold[11] .

A   **B**

C   **D**
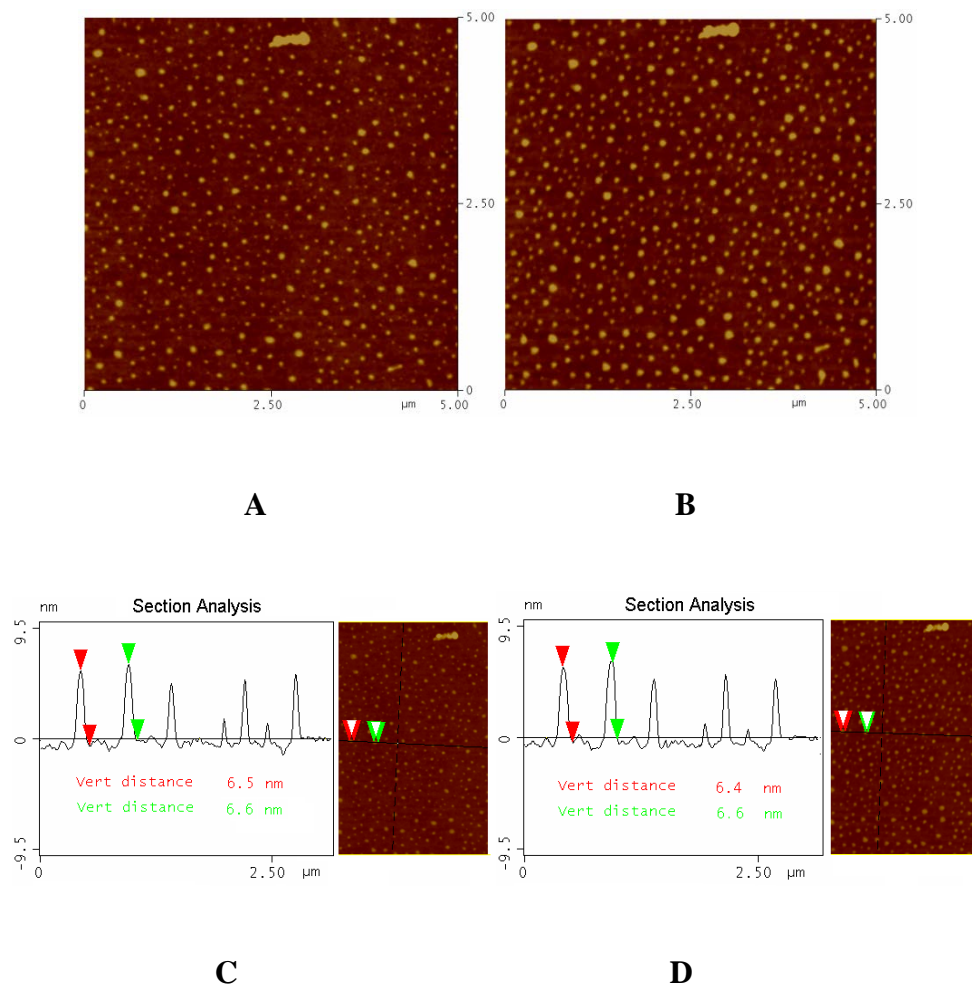
Figure S3. The AFM image (tapping, height) of 15 nm polystyrene film spin-coated on silicon wafer with nanoprotrusions formed by standard immersion/pressure drop procedure described in the paper (pressure drop ~10 kPa/5 sec applied on the sample immersed in deionized water). The AFM image of identical location shows nanoprotrusions as received (A), after 2 hours drying in vacuum dryer (50 Pa/25°C) (B). Corresponding profile (line) analyses are shown in Figures (C, D), where red and green marks point to identical nanoprotrusion heights.

3. The water-immersion stability of polystyrene film

The stability of the film upon simple water immersion (i.e. omitting pressure drop) tested under experimental conditions identical to those utilized for nanostructuring experiments showed no change of surface nanomorphology of both thin ($\geq$ 15 nm) and ultrathin ($\leq$ 5 nm) polystyrene film as illustrated by Fig. 7. This finding, which is in agreement with results obtained on other materials[11], proves besides significance of pressure drop for nanostructuring process also stability of silicon wafer-supported polystyrene film – both ultrathin and thin - during water immersion.

Extended stability test performed on larger area of polystyrene film by its simple water immersion prolonged to 100 minutes showed also good overall film stability without any alteration of surface morphology as illustrated by in situ optical microscopy image (Figure S4).

Conclusively, the polystyrene film spin-coated on silicon wafer shows both short and long-term stability upon prolonged water immersion, which makes adverse effects of detachment and blistering[12] unlikely.

| A | B |
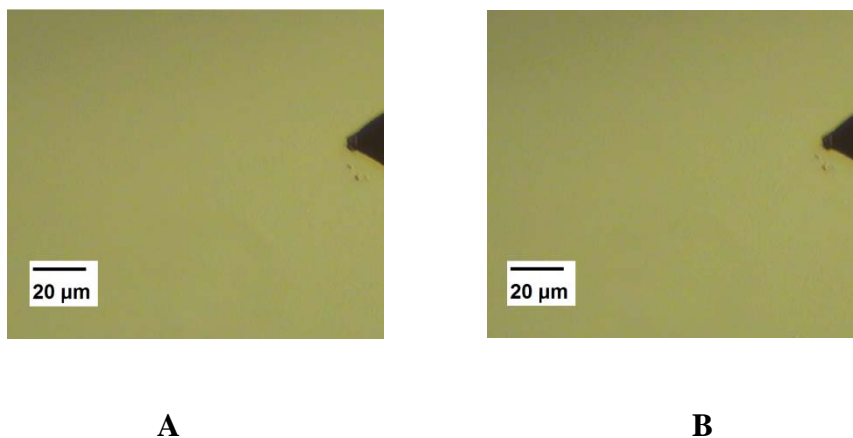
Figure S4. Optical in-situ images of 15 nm thin polystyrene film spin coated (0.2% w/w solution, 500 rpm) from its toluene solution on silicon wafer. Images acquired immediately after surface immersion in deionized water (A) and after 100 min of immersion (B) show that the film remains intact during simple immersion. Dark triangle on the right side of the image is the top of AFM cantilever serving as a pointer (for the detailed comparison note two defects in the film located nearby the cantilever top). The experiment was performed in the AFM cell for imaging in liquids, water temperature was 20°C.

4. Nanobubble and nanoprotrusion/nanopinhole assembly assessment

As we have already noticed, certain discrepancy exists between dimensional distribution of surface nanobubbles and nanoprotrusions formed upon application of water-immersion/pressure drop procedure ("…*nanopattern dimensions are well below the corresponding nanobubble size distribution range…*"[11]). Though this finding supports presented model of nanoprotrusion/nanopinhole formation within the narrow foot−neck region of surface nanobubble, further discrepancy exists between nanobubble and nanopattern appearance

statistics: While appearance density number of nanopinholes, formed under conditions of our experiment, approaches $700/\mu m^2$ with surface coverage fraction at 25% and for nanoprotrusions at thick PS film this number is close to $800/\mu m^2$ (surface coverage over 30%), the maximum resolvable number of nanobubbles in dense assembly reaches up to $200/\mu m^2$ (with typical value at $160/\mu m^2$) and surface fraction coverage over 30%, reflecting noticeable nanobubble broadening effect. Though caution should be kept concerning above mentioned numbers, which involve AFM tip convolution, we end up with some nanobubble deficiency, anyway. Two explanations can be considered:

(i) Some nanobubbles active in nanostructuring are not present on the surface at the time of AFM imaging.

To justify this point, it should be noted, that in situ AFM imaging is always performed at stationary, equilibrated conditions (stagnant liquid) required for undisturbed, stable AFM image acquisition; the nanostructuring process itself is not accessible for AFM imaging due to cantilever excessive swings induced by liquid flow and pressure drop. Thus, the cantilever is disengaged during pressure drop period to prevent its damage.

(ii) Not all nanobubbles engaged in nanostructuring process are resolved by AFM imaging.

Now we can examine feasibility of both above mentioned variants:

Ad (i). Let's consider that appearance density number of surface nanobubbles observed by AFM is correct. Then it is more than 3 times lower than the appearance density number of nanopinholes and nanoprotrusions. Utilizing Henry's law[13], we can elucidate that the pressure

drop -10 kPa applied on aqueous phase saturated by air under normal atmospheric conditions (101 kPa, 20 °C) causes its oversaturation by about 3 mg/L (air is approximated by 0.21 O_2/0.79 N_2 mixture). As the pressure drop is accompanied by the aqueous phase flow at the speed 10^{-2} ms^{-1} with low Re ≈ 10, the majority of the experimental cell cavity falls within boundary layer region. The gas surplus feeds the nanobubble nucleation process, which, under such mild conditions is assumed to take prevailingly heterogeneous path requiring lower gas supersaturation than homogeneous nucleation[14]. As the heterogeneous nucleation is expected to originate from stabilized gas nanopockets (nuclei) trapped in surface hydrophobic nanocavities[15,16], where the lower effective surface energy diminishes free energy barrier, it proceeds in the stationary layer adjacent to the solid surface, where the flow speed drops to zero and nanobubble pinning, ranked besides oversaturation as a fundamental prerequisite for surface nanobubble existence[17-19], takes place. Thus, in simplified example considering dynamic equilibrium nanobubble model[20], water oversaturation by -10 kPa pressure drop and stationary diffusion[21] from 10 µm layer (time scale ~10^{-2} sec) could provide gas excess for up to 10^3 surface nanobubbles per $µm^2$ (assuming nanobubble average radius 100 nm and 10 nm apex height). Thus increasing population of nanobubbles "pre-existing" on PS surface upon its water immersion due to incomplete wetting[22], by nanobubbles heterogeneously nucleated by pressure drop period, appears to be feasible.

Ad (ii). Besides tip-nanobubble interactions which affect both nanomorphology and resolution, as discussed in Paragraph **1,** there are resolution-limiting criteria related to nonlinear nature of the AFM imaging: While convolution of AFM tip with scanned object causes its profile modification and broadening, the AFM lateral resolution is affected by the height difference between adjacent objects (see e.g. ref. [23]) according to spatial resolution formula $\boldsymbol{d} = \sqrt{(8\boldsymbol{R}\Delta\boldsymbol{h})}$,

where d is resolved object distance, Δh is the objects height difference and R stands for the AFM tip radius. Thus for 10 nm height difference and declared tip radius 50 nm, resolution of adjacent solid objects is limited to less than 60 nm, while for ultrasharp AFM tip R = 20 nm it may reach value d = 40 nm, below which all adjacent objects are imaged as one. This factor gains even higher importance for scanning soft materials like nanobubbles, where the tip sharpness does not translate into the resolution enhancement. Comparing distribution curves of nanobubbles and nanoprotrusions by the height spread (Δh) expressed as half maximum width of height distribution peak, the spread Δh = 10 nm for nanobubbles and Δh = 3 nm for nanoprotrusions was found (for nanopinholes the convolution with AFM tip creates artefact due to limitation by the tip penetration depth; thus the comparison would not be informative). Significant, though somewhat less pronounced, is the radius spread difference yielding 50 nm and 20 nm radius spread for nanobubbles and nanoprotrusions, respectively, reflecting possibly certain equalizing effect of tip convolution.

The AFM image evaluation by threshold procedure makes nanobubble numbers further underestimated[8] : The appearance density number of nanobubbles within the assembly is reduced to n = 50/μm^2 with coverage exceeding 30%, compared to boundary-based evaluation yielding typical value n = 160/ μm^2 in the same image area. Apparently both nanobubble interaction with AFM tip and AFM resolution limits lead to lower apparent nanobubble appearance density and higher surface coverage numbers compared to reality, thus the exact determination of nanobubble numbers in dense assemblies is always burdened by a negative error.

   As both above mentioned variants (i), (ii) act in accord, the nanobubble number density acquired from in situ AFM image before application pressure drop can be significantly lower, than the number of nanobubbles virtually acting in nanostructuring process. Consequently,

excess nanoprotrusion and nanopinhole density number, compared to nanobubble numbers, is noticed.

Fundamental restrictions exist both in AFM modus operandi and in experiment requirements, which prevent full resolving of dynamics of nanostructuring phenomenon within the scope of present instrumentation. Noncontact, fast, high resolution optical imaging[24], which would help to resolve gaseous nanodomain-related phenomena, is restricted by so far relatively low (~300 nm) resolution limit.

5. Influence of compounded AFM tip-nanobubble interaction on nano-indent formation

To complete the story, we have to mention also the nanoindentation effect, which was found to accompany the *in situ* AFM imaging of surface nanobubbles. We have already reported on surface rearrangement taking place on water immersed basal plane HOPG, imaged by AFM *in situ*, explained by nanobubble-assisted exfoliation[1] and circular rims formed around each nanobubble perimeter upon prolonged AFM scanning. Similar effect was reported by Wang, Bhushan *et al.*[25] as rimmed nanoindents emerging slowly during hours-long AFM scanning of nanobubbles on water-immersed polystyrene surface. The effect was ascribed to internal nanobubble pressure and horizontal force component of nanobubble surface tension, which magnitude exceeds the strength of surface layer, causing its local rupture. Closer examination, however, revealed that the duration of AFM scanning and the pressure applied on the AFM tip play the key role in the nanoindent development. While at regular setpoint amplitude forces below 200 pN (OTESPA cantilevers) can be applied to reach stable imaging, the rim visibility depends on the amplitude setpoint and thus on the pressure imposed by the AFM tip on nanobubble surface.[1] Besides the rim formation, the bowl-like concave nanostructure appears at the nanobubble location during continuous AFM scanning (Figure S5).

We can assume that compounded tip-nanobubble and nanobubble-substrate interaction is the cause for this phenomenon.

In accordance with observation of nanobubble movement[11] and elastic deformation[3,26,27] by interaction with AFM tip[5] during scanning, the following scenario, considering hydrophilic AFM tip, can be drawn (Figure S6): Repeated cyclic movement of tapping AFM tip on nanobubble surface causes periodic compression and expansion of nanobubble sphere as well as lateral movements and deformation of nanobubble contact line, causing also hiding (at lower applied forces/higher tapping amplitude) and revealing (at about 10% lower tapping amplitude, *i.e.* at higher force applied on tip) surface patterns near the nanobubble perimeter (Figure S6 E).
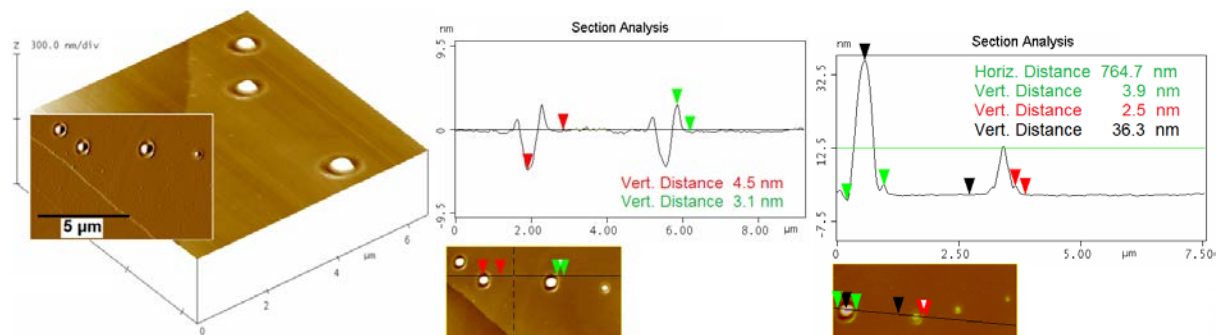
Figure S5. *In situ* AFM image (tapping, height) of concave bowl-like nanostructures surrounded with circular rims developed during 1 hour long continuous scanning of nanobubbles on basal plane HOPG surface in deionized water. The 3D height (left) and top view amplitude (insert) images with corresponding profile (line) analyses of bowl-rim (middle) and whole structure with nanobubbles (right) are shown. Black, red and green arrows indicate vertical and horizontal dimensions.
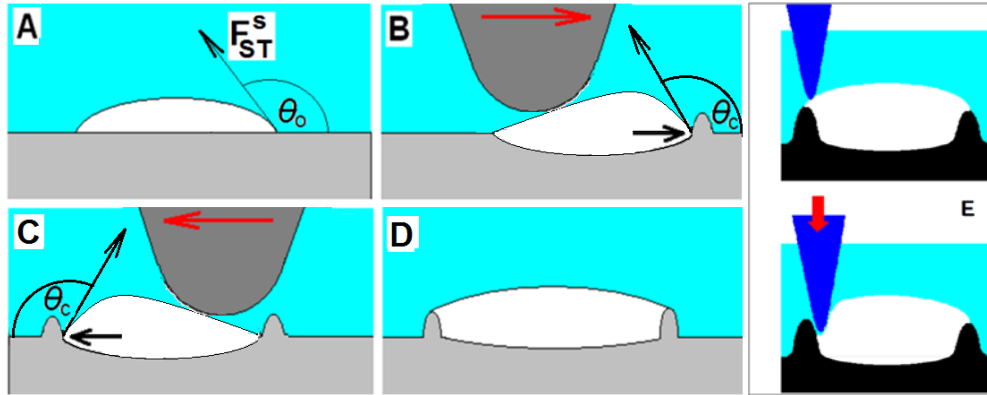
Figure S6. Schematic drawing of suggested mechanism of rim-bowl formation in solid substrate by the tip-nanobubble-substrate interaction during AFM scanning (A-D) showing different stages of rimmed bowl formation from intact (A) to final concave nanopattern (D) and illustration of hiding and reappearing of rim image (E) upon nanobubble deformation by rising (top) and lowering (bottom) AFM tip. Parameters involved in tip-nanobubble-substrate interaction are F_{AFM} force imposed by the scanning tip (vertical red arrow), p, Δp external pressure, internal-external pressure difference, F_P force developed on the nanobubble contact line due to internal pressure and Θ_0, Θ_C nanobubble contact angle at rest and compressed by the tip respectively, which corresponds to advancing contact angle of pinned nanobubble. Horizontal red arrows (B, C) indicate scanning directions.

Besides its influence on imaging, scanning AFM tip causes periodic movement of nanobubble interface, which decelerated by its pinning[17,28] transduces interfacial force to solid substrate and develops tension stress in its surface layer.[11] Consequently, the lateral (F_L) and perpendicular (F_P) components of interfacial (tension) force are modulated

$$F_L = F_{ST} \cos(180 - \Theta) \text{ and } F_P = F_{ST} \sin(180 - \Theta) \quad (5)$$

in accordance with contact angle Θ ranging from advancing - compressed (Θ_C) to receding or relaxed (Θ_0) value.

The tension stress $\sigma = \Gamma_{WA} \cos (180 - \Theta)/h$ induced in solid by contact line is primarily determined by the water-air surface tension Γ_{WA} and layer thickness h (see above). As these forces do not exceed the strength of graphene,[1] tearing and fragmentation of graphene basal plane take place presumably on its defects. The combination of periodic lateral and axial movements of nanobubble driven by scanning AFM tip generates thus "milling" forces acting at the nanobubble contact line (Figures S6 B-D), forming concave rounded pattern (Figures S5, S6 E). This slow process is well followed *in situ* by AFM, which at the same time supplies the driving force. Besides force developed by scanning AFM tip, the long scanning period at long wetting time may co-act in rim development besides bubble-tip interaction. Though capillary forces are too weak to exhibit their influence on solid surface during short period of wetting/pressure drop experiment, they can initiate polymer creep ("cold flow") at long wetting times, i.e. long exposition to capillary forces acting at bubble ternary interface. As elastocapillarity itself is known to create circular rims at surface droplet and bubble boundary[29], it can also contribute to creation circular rims observed during long continuous scanning of surface bubbles.

REFERENCES

(1) Janda, P.; Frank, O.; Bastl, Z.; Klementová, M.; Tarábková, H.; Kavan, L.: Nanobubble-Assisted Formation of Carbon Nanostructures on Basal Plane Highly Ordered Pyrolytic Graphite Exposed to Aqueous Media. *Nanotechnology* **2010**, *21*, 095707−095714.

(2) Thormann, E.; Simonsen, A. C.; Hansen, P. L.; Mouritsen, O. G. Force Trace Hysteresis and Temperature Dependence of Bridging Nanobubble Induced Forces between Hydrophobic Surfaces. *ACSNano* **2008**, *9*, 1817–1824.

(3) Zhao, B.; Song, Y.; Wang, S.; Dai, B.; Zhang, L.; Dong, Y.; Lü, J.; Hu, J. Mechanical mapping of Nanobubbles by Peak Force Atomic Force Microscopy. *Soft. Matter*. **2013**, *9*, 8837–8843.

(4) Peng, H.; Hampton, M. A.; Nguyen, A. V. Nanobubbles Do Not Sit Alone at the Solid−Liquid Interface. *Langmuir* **2013**, *29*, 6123−6130.

(5) Walczyk, W.; Hain, N.; Schönherr, H. Hydrodynamic effects of the tip movement on surface nanobubbles: a combined tapping mode, lift mode and force volume mode AFM study. *Soft. Matter*. **2014**, 10, 5945-5954.

(6) MultiMode SPM Instruction Manual (Digital Instruments/Bruker), V.4.22, 8-26.

(7) Walczyk, W.; Schönherr, H. Dimensions and the Profile of Surface Nanobubbles: Tip−Nanobubble Interactions and Nanobubble Deformation in Atomic Force Microscopy. *Langmuir* **2014**, *30*, 11955−11965.

(8) Wang, Y.; Wang, H.; Bi, S.; Guo, B. Automatic morphological characterization of nanobubbles with a novel image segmentation method and its application in the study of nanobubble coalescence. *Beilstein J. Nanotechnol.* **2015**, *6*, 952–963.

(9) Bhushan, B.; Wang, Y.; Maali, A. Coalescence and movement of nanobubbles studied with tapping mode AFM and tip−bubble interaction analysis. *J. Phys.: Condens. Matter.* **2008**, *20*, 485004.

(10) Li, D.; Jing, D.; Pan, Y.; Wang, W.; Zhao, X. Coalescence and Stability Analysis of Surface Nanobubbles on the Polystyrene/Water Interface. *Langmuir* **2014**, *30*, 6079 – 6088.

(11) Tarábková, H.; Bastl, Z.; Janda, P. Surface Rearrangement of Water-Immersed Hydrophobic Solids by Gaseous Nanobubbles. *Langmuir* **2014**, *30,* 14522−14531.

(12) Berkelaar, R. P.; Bampoulis, P.; Dietrich, E.; Jansen, H. P.; Zhang, X.; Kooij, E. S.; Lohse, D.; Zandvliet, H. J. W. Water-induced blister formation in a thin film polymer. *Langmuir* **2015**, *31*, 1017–1025.

(13) Sander, R. Compilation of Henry's law constants (version 4.0) for water as solvent. *Atmos. Chem. Phys.* **2015**, 15 , 4399–4981.

(14) Apfel, R. E. Vapor nucleation at a liquid-liquid interface. *J. Chem. Phys.* **1971**, *54,* 62–63.

(15) Borkent, B. M.; Gekle, S.; Prosperetti, A.; Lohse, D. Nucleation threshold and deactivation mechanisms of nanoscopic cavitation nuclei. *Phys. Fluids* **2009**, *21*, 102003.

(16) Blatteau, J.E.; Souraud, J.B.; Gempp, E.; Boussuges, A. Gas nuclei, their origin, and their role in bubble formation. *Aviat. Space Environ. Med.* **2006**, *77*, 1068-1076.

(17) Zhang, X.; Chan, D. Y. C.; Wang D.; Maeda, N. Stability of interfacial nanobubbles. *Langmuir* **2013**, *29*, 1017−1023.

(18) Liu, Y.; Zhang, X. A unified mechanism for the stability of surface nanobubbles: Contact line pinning and supersaturation. *J. Chem. Phys.* **2014,** *141*, 134702.

(19) Lohse, D.; Zhang, X. Pinning and gas oversaturation imply stable single surface nanobubbles. *Phys. Rev. E* **2015,** *91*, 031003(R).

(20) Brenner, M.P.; Lohse, D. Dynamic equilibrium Mechanism for Surface Nanobubble Stabilization. *Phys. Rev. Lett.* **2008**, *101*, 214505.

(21) Ferrell, R. T.; Himmelblau, D. M. Diffusion Coefficients of Nitrogen and Oxygen in Water. *J. Chem. Eng. Data* **1967,** *12* , 111 – 115.

(22) Simonsen, A. C.; Hansen, P. L.; Klösgen, B. Nanobubbles Give Evidence of Incomplete Wetting at a Hydrophobic Interface. *J. Colloid Interf. Sci.* **2004**, *273*, 291–299.

(23) García, R. Amplitude Modulation Atomic Force Microscopy. Chapter 8.2.2 Lateral Resolution, John Wiley & Sons, 2011.

(24) Karpitschka, S.; Dietrich, E.; Seddon, J. R. T.; Zandvliet, H. J. W.; Lohse, D.; Riegler, H. Nonintrusive Optical Visualization of Surface Nanobubbles. *Phys. Rev. Lett.* **2012,** *109,* 066102.

(25) Wang, Y.; Bhushan, B.; Zhao, X. Nanoindents Produced by Nanobubbles on Ultrathin Polystyrene Films in Water. *Nanotechnology* **2009**, *20,* 045301−045306.

(26) Walczyk, W.; Schönherr, H. Characterization of the Interaction between AFM Tips and Surface Nanobubble. *Langmuir* **2014**, *30,* 7112−7126.

(27) Walczyk, W.; Schön, P. M.; Schönherr, H. The Effect of PeakForce Tapping Mode AFM Imaging on the Apparent Shape of Surface Nanobubbles. *J. Phys. Condens. Matter.* **2013**, *25*, 184005.

(28) Liu, Y.; Zhang, X. Nanobubble Stability Induced by Contact Line Pinning. *J. Chem. Phys.* **2013**, *138*, 014706.

(29) Das, S.; Marchand, A.; Andreotti, B.; Snoeijer, J. H. Elastic Deformation due to Tangential Capillary Forces. *Phys. Fluids* **2011**, *23*, 072006.